Author/s:
Philpott, L;Johnson, BC;Fronzi, M;Rokhsat, E;Luo, W;Hutchison, J;Wibowo, AA;Delaney, R;Bullock, J

Title:
Strain-Dependent Photodetection with Layered InSe Photoconductors

Date:
2025-06-18

Citation:
Philpott, L., Johnson, B. C., Fronzi, M., Rokhsat, E., Luo, W., Hutchison, J., Wibowo, A. A., Delaney, R. & Bullock, J. (2025). Strain-Dependent Photodetection with Layered InSe Photoconductors. Nano Letters, 25 (24), pp.9526-9534. https://doi.org/10.1021/acs.nanolett.5c00396.

Persistent Link:
https://hdl.handle.net/11343/362901

Strain-dependent photodetection with layered InSe photoconductors

Luke Philpott[1], Brett C Johnson[2], Marco Fronzi[3,4], Eliza Rokhsat[5], Wei Luo[5], James Hutchison[5], Ary Anggara Wibowo[6], Robert Delaney[1], James Bullock[1]*

[1.] Department of Electrical and Electronic Engineering, University of Melbourne, Parkville, VIC 3010, Australia

[2.] School of Science, RMIT University, Melbourne, VIC 3001, Australia

[3.] School of Chemical and Biomedical Engineering, University of Melbourne, Parkville, VIC 3010, Australia

[4.] School of Physics, The University of Sydney, Camperdown, NSW 2050, Australia

[5.] School of Chemistry and Centre of Excellence in Exciton Science, The University of Melbourne, Parkville, Victoria, 3010, Australia

[6.] School of Engineering, The Australian National University, Canberra, Australian Capital Territory, 2601, Australia

* James Bullock: E-mail: james.bullock@unimelb.edu.au

Keywords

2D materials, InSe, flexible devices, strain tuning, bandgap engineering

Abstract

Controlled bandgap modulation is of particular interest for next generation optoelectronic devices, allowing the development of ‘active’ or ‘reconfigurable’ detectors and emitters. In van der Waals layered semiconductors, which exhibit high strain tolerance, strain has become a notable tool for active bandgap tuning. In this work, we demonstrate a flexible bulk InSe gated photoconductor with strain-induced modulation of the bandgap energy, shifting to higher and lower energies under compression and tension, respectively. Photoluminescence measurements reveal shift rates of around 117.1 meV·%$^{-1}$ in tension, and 107.6 meV·%$^{-1}$ in compression. Spectral responsivity measurements indicate smaller shift rates, likely due to non-uniform strain application. Notably, these flexible devices achieve impressive performance with specific detectivities up to 3.78×10^{12} cm·Hz$^{1/2}$·W^{-1}, a rise time of 4.1 μs, and a responsivity of 1.25×10^{3} A·W^{-1}. The realisation of high responsivity and fast response times underscores the potential of this device architecture for advanced optoelectronic applications.

Van der Waals (vdW) materials, such as transition metal dichalcogenides and graphene, have emerged as promising candidates for optoelectronic applications [1-5]. Their appeal largely stems from their unique properties such as strong optical absorption and near-unity photoluminescence quantum yields [6, 7], particularly in monolayer and few-layer forms [8]. A less explored sub-set of vdW materials, the III-VI vdW semiconductors GaSe and InSe, retains excellent optoelectronic properties even in their bulk form. InSe, in particular, has gained significant interest due to its scalable growth [9, 10], high photoluminescence quantum yield [11], ballistic transport [12], and second-harmonic generation [13].

The bandgap of InSe varies from an indirect ~2.4 eV gap in its monolayer form, to a direct ~1.3 eV gap in its bulk form, making it a promising candidate for visible to near infrared (NIR) optoelectronic applications [14, 15]. Bulk InSe photodetectors have already demonstrated high responsivities, reaching up to 10^8 $A \cdot W^{-1}$, at λ = 450 nm [16-18]. Additionally, the bandgap of bulk InSe can be actively tuned via the application of strain. Studies on flexible substrates have shown that its peak photoluminescence (PL) emission can be reversibly redshifted by 57-154 $meV \cdot \%^{-1}$ under tensile strain [19, 20], and blue-shifted by 100-140 $meV \cdot \%^{-1}$ under compressive strain [20]. This strain-tunability has been leveraged to develop photodetectors with adjustable spectral response and responsivity [21, 22]. However, as shown in Table 1, flexible InSe-based devices have yet to match the performance of devices formed on rigid substrates, particularly at the band edge of bulk InSe. The table summarizes key performance metrics for a selection of flexible vdW material photodetectors measured under strained conditions.

In this work, we demonstrate a strain-tunable InSe gated photoconductor on a flexible substrate, achieving a highest-in-class responsivity of 1.25×10^3 $A \cdot W^{-1}$ and a fast rise time of 4.1 μs, setting a benchmark for flexible bulk InSe photoconductive devices. We quantify the strain-induced band edge shifts using PL and spectral photoresponse measurements, observing shift rates up to 117.1 $meV \cdot \%^{-1}$ under tensile strain and 107.6 $meV \cdot \%^{-1}$ under compressive strain. These results highlight the substantial potential of strain-tuneable bulk InSe-based optoelectronics.

Gamma-phase InSe has a rhombohedral layered structure with a R3m space group, as shown in Fig. 1a. The bandgap of this material undergoes broadening (narrowing) under compressive (tensile) strain, as verified in experiments [20, 23], and through simulations (see Supporting Information S1). To experimentally test the magnitude of this strain-dependent behaviour, we first measure InSe's PL as a function of strain. We utilise bulk InSe flakes (2Dsemiconductors, Bridgman growth) with an average optical lifetime of 9.4 ns, and thicknesses ranging between 50-300 nm (see Supporting Information S2 and S3). This thickness range was chosen to

maximise light absorption in later photoconductive devices (see Supporting Information S4). Previous studies have also concluded that InSe's strain dependent band gap shift begins to saturate at bulk thicknesses above ~20 nm [20], and that for bulk InSe flakes of ~100 nm the binding energies are lower than the thermal energy at room temperature, indicating a free carrier dominated system [11]. The bulk flakes used in this study are mechanically exfoliated from a bulk crystal, onto a 1 μm thick polymethyl methacrylate (PMMA) film which is layered onto the surface of an 0.8 mm polyimide substrate. PMMA is used to ensure good strain transfer efficiency [23, 24]. Strain is applied to the substrate and InSe flake via a two-point bending method, as shown in Fig. 1b. This method has been used in similar studies in the past [25-27], however, some limitations have been reported including slippage between the 2D material and the substrate [24], and uncertainty as to the onset of strain application. To address these limitations, we used calculated strain values at 0% and ~0.8% strain to extract the shift rates, as we find this to be the most accurate region (see Supporting Information S5).

To probe the change in the bandgap with strain, the PL of multiple flakes were measured between 0% to 1%, taken using a Horiba Synapse InGaAs/Symphony system with a λ = 785 nm illumination laser. Representative PL spectra are provided in Fig. 1c for tensile strain with the unstrained PL peak position centred around 1.26 eV, in line with previous studies [20, 23]. The shift rate in the PL peak position under tensile strain is found to be 74.4±2.1 meV·%$^{-1}$ in a redshift direction. The repeatability of this behaviour is confirmed in Fig. 1d, in which 0.7% tensile strain was applied to a representative sample 100 times, with the PL being captured after every tenth application of strain. Fig. 1e shows the PL spectra of a representative InSe flake as a function of compressive strain ranging between 0% to 1%, with a resultant blueshift of 93.0±3.1 meV·%$^{-1}$.

To support these results, Fig. 2a shows the experimentally observed peak shift with tensile strain from the centre of several randomly oriented and different thickness bulk InSe flakes. It shows that the peak shift is relatively consistent and does not depend heavily on the angle between the bending axis and InSe's crystal orientation. From these measurements, the average shift rate under tensile strain is 84.6 meV·%$^{-1}$, with values between 74.4 meV·%$^{-1}$ and 117.1 meV·%$^{-1}$ measured from different flakes, agreeing with ranges reported in literature of 57-154 meV·%$^{-1}$ [19, 20].

Further PL investigation was performed using hyperspectral imaging on a representative thick InSe flake (shown in Fig. 2b), to understand how the entire flake is influenced by strain. These measurements were taken using a Photon Etc. IMA hyperspectral imaging system including a ZephIR 1.7 InGaAs camera and a λ = 463 nm diode laser illumination source. Fig. 2c shows the PL peak position map across this flake, showing a substantial variation in local strain

across the flake under both compressive and tensile strain. At 0% strain, there is a mostly uniform PL peak across the entire flake, with emission close to the bulk unstrained InSe PL emission of 980 nm (1.26 eV). At both -1% and 1% strain, the edges of the flake retain values near the unstrained PL emission peak, whilst the centres of both images show strong shifts. These centres are at λ = 900 nm (shift rate of 107.6 meV·%$^{-1}$ from -0.8% to 0%) for compressive strain and λ = 1040 nm (shift rate of 89.0 meV·%$^{-1}$ from 0% to 0.8%) for tensile strain. The tensile PL peak positions from the centre of the flake are also included in Fig. 2a. The underlying mechanism for the regionality of the strain is likely associated with incomplete adhesion to the substrate at the flake edges [28]. Notably, at the boundary of the flake there is additional broader PL emission resulting from the sample's emission outcoupling to the flake edge. An accompanying mapping of InSe's A^1_{1g}, A^2_{1g} and E^1_{2g} Raman peaks across another bulk flake, showed shift directions under strain consistent with previous reports, but did not provide enough resolution to distinguish regional variation (see Supporting Information S6).

Next, to investigate the impact of strain on InSe photodetection in the NIR we fabricate gated photoconductors on flexible substrates, a device schematic of which is shown in Fig. 3a. The InSe photoconductors were fabricated on polyimide sheets with a thickness of 0.8 mm. Shadow masks were used to define source, drain and gate contacts. The gate contact consisted of a stack of Ti (5 nm) and Ni (60 nm) deposited via electron-beam and thermal evaporation, respectively. A PMMA (1 μm) gate insulator was subsequently spin-coated and cured onto the substrate followed by mechanical exfoliation of the InSe channel, and then thermal evaporation of the Ni (80 nm) source/drain contacts. Ni was chosen as it adhered well to the PMMA surface and produced consistent Ohmic contacts to InSe. These contacts also influence how strain is transferred to the material as the flake is fixed to the substrate at the Ni contacts. Fig. 3b shows an optical microscope image of a representative device highlighting the areas of InSe (red) and Ni (blue). Fig. 3c shows an atomic force microscope (AFM) topological image of the edge of this flake, where the step-height was ~270 nm, as plotted in Fig. 3d.

Following fabrication, the devices were electrically characterised with a Keysight B1500A semiconductor device parameter analyser by measuring the drain current (I_D) versus gate voltage (V_G) and I_D versus drain voltage (V_D) behaviour. Fig. 3e shows the I_D-V_D characteristic of a representative device and how the Ni front electrodes were able to form Ohmic contacts with the InSe flake. Fig. 3f shows the I_D-V_G behaviour in both the dark (dashed lines) and in the light (solid lines) when illuminated with a visible light lamp (~10 mW·cm^{-2}). Clear n-type behaviour can be seen with the dark current reaching a minimum at higher negative gate voltages. Furthermore, an on/off ratio of ~10^6 was measured in dark conditions when biased at V_D = 100 mV.

To analyse the InSe photoconductor's performance, representative devices were characterised under modulated λ = 685 nm and λ = 980 nm laser illumination. The device's photoresponse was captured, after amplification via a transimpedance amplifier (SR570), on an oscilloscope. The InSe photoconductor's photoresponse speed, shown in Fig. 4a, displays a rise time of 4.1 μs and a fall time of 10.2 μs with illumination from a modulated λ = 639 nm laser, corresponding to an RC limited bandwidth of ~34kHz. These rise/fall times were measured between 10-90% of the on/off current when biased at V_D = 100 mV and no V_G applied. These results are among the fastest response times reported in the literature for InSe photodetectors [21, 29]. The intensity dependent responsivity and detectivity were next investigated at λ = 639 nm. The responsivity values were calculated from the measured photocurrent divided by the incident light intensity. Where the incident power was determined using a calibrated germanium detector (FDG03-CAL) with known responsivity. Detectivity was calculated by using the estimated shot noise from the measured dark current (see Support Information S7). These measurements, shown in Fig. 4b, are taken at differing gate biases (V_G = -40 to 40 V) with a constant V_D = 100 mV. At a gate voltage of V_G = 20 V, the highest responsivity of 1.25×10^3 $A\cdot W^{-1}$ was measured at an incident power of 767 $nW\cdot cm^{-2}$. The magnitude of the responsivity confirms the presence of gain, which is discussed in Supporting information S8. A maximum specific detectivity of 3.78×10^{12} $cm\cdot Hz^{1/2}\cdot W^{-1}$ was achieved under these same conditions. We note that this detectivity should be taken as an upper limit estimate due to utilising the calculated shot noise from the device's dark current. In reality, 1/f noise can also contribute to the noise behaviour of photoconductive devices, particularly at low frequencies [30, 31]. However, at frequencies close to the bandwidth of InSe the shot noise is found to be a reasonable estimate of total noise (see Supporting Information S7). Regardless, these results compare well to other flexible devices in the recent literature, showing the highest responsivity and detectivity values compared to other InSe based flexible devices [21, 22]. The improved responsivity is partially attributable to the increased absorption due to the use of thicker InSe photoabsorbers relative to previous studies. The decrease in responsivity with increasing illumination intensity is common for nanomaterial detectors and has been explained by the saturation of trap states, which affects the photoconductive gain [18, 32-38]. The exception to this behaviour, seen for strong negative gate biases, may be associated with the gate and injection dependence of quantum efficiency/gain within the InSe absorber [39, 40]. Another set of measurements, shown in Fig. 4c were taken under λ = 980 nm illumination, which is close to InSe's unstrained band edge. The best responsivities and detectivities obtained at λ = 980 nm were 89 $A\cdot W^{-1}$ and 2.71×10^{11} $cm\cdot Hz^{1/2}\cdot W^{-1}$, respectively, both of which were measured under low intensity (2.2 $\mu W\cdot cm^{-2}$) with V_G = 20 V. This lower responsivity at λ = 980 nm versus λ = 639 nm is likely a consequence of InSe's lower absorption coefficient at its band edge (see Supporting Information S8).

This lower absorption/photoresponse around the band edge can be modulated with strain, and as such we next measured the strain-dependent spectral responsivity. Representative devices were measured on a custom-built dispersive visible-NIR characterisation platform (see Supporting Information S8). Figure 5a and 5b show the changes in normalised spectral responsivity as a function of tensile/compressive strain for two devices, with the black curves being representative of 0% strain in both plots. Normalisation was performed using the peak value within the range of 1.2-1.3 eV, although only minor changes in the global photoresponse magnitude are noted without normalisation (see Supporting Information S9). In Fig. 5a, devices are measured under tensile strain ranging from 0% to 1.1%, operating with V_G = 20 V. A clear redshift in the band edge can be seen with increasing tensile strain, with a shift rate of 44.5±1.5 meV·%$^{-1}$. The bandgap was estimated by making fits to the external quantum efficiency (EQE) band edge using a previously reported technique [41]. In addition to the translation of the band edge position to lower energy values, a reduction in the gradient of the band edge was also seen under strain values above 0.8%. This may be due to different regions of the device exhibiting different absorption behaviour due to non-uniform strain. The inset of Fig 5a shows the enhancement in responsivity as a function of wavelength when switching between 0% and 1% strain, with a peak enhancement around 1.1eV. At this wavelength, the photoresponse is enhanced by almost two orders of magnitude, demonstrating effective photoresponse modulation. In Fig. 5b, devices were measured under compressive strain with a floating back gate and V_D = 500 mV. A minor blueshift is seen with a band edge shift rate of 35.1±4.6 meV·%$^{-1}$. The smaller strain rates relative to the earlier PL analysis is likely at least partially due to non-uniform strain effecting the spectral responsivity (which collects current from the entire device) to a greater degree than the PL measurements (which samples a smaller region of a given flake).

Another representative device was used in Fig. 5c for repeatability testing of the InSe photoconductors under multiple cycles of tensile strain. The device was strained from 0% to 0.7% 1000 times, showing very consistent responsivity up to 800 cycles. The spectral responsivity drops after 900 cycles, due to visible damage to the metal contacts, which could be improved by using different contacting schemes. Regardless, this test demonstrates the durability of the InSe photoconductor's responsivity even without consideration for device longevity. Multiple strategies could be implemented to improve device endurance, and strain uniformity. Encapsulation may help by protecting the contacts, enhancing strain uniformity, limiting oxidation, and preventing wrinkling of the InSe. Similarly, the use of adhesion promoters, such as (3-aminopropyl)triethoxysilane or poly-l-lysine, could also be used to improve flake adhesion and strain uniformity. Another issue relevant to InSe, is surface oxidation which can lead to performance degradation for thin devices [42]. However, given the

focus on thick InSe photoabsorbers in this study, and the fact that InSe's surface oxide can be made self-limiting [43], we do not anticipate this to be a major problem (see Supporting Information section S10).

Finally, Fig. 5d summarises the results of this study, plotting the estimated bandgap extracted from the PL and spectral responsivity measurements. All datasets show a clear trend of increasing/decreasing bandgap energy with compressive/tensile strain. As discussed above, the lower strain rates seen from spectral responsivity measurements is likely a consequence of being large area measurements, and that more uniform strain application could improve the observed band edge shift. Regardless, these results demonstrate effective modulation of the band edge and show promise for the future of strain tuneable bulk InSe optoelectronic devices for visible to NIR applications. This includes use for single pixel spectroscopy by leveraging the changing photoresponse profile with respect to strain to perform spectral reconstruction around InSe's band edge [44]. Switching to miniaturised strain application platforms, such as by using arrays of micro-electro-mechanical actuators, could also introduce other applications, such as reconfigurable imaging.

This study investigated the effect of strain on InSe's bandgap through PL peak position and spectral responsivity measurements. PL measurements revealed significant PL peak position shift rates of 117.1 $meV \cdot \%^{-1}$ under tension and 107.6 $meV \cdot \%^{-1}$ under compression. Spectral responsivity measurements, taken on gated, flexible InSe photoconductors, showed smaller band edge shift rates of 44.5 $meV \cdot \%^{-1}$ and 35.1 $meV \cdot \%^{-1}$ for tensile and compressive strain, respectively. These flexible InSe photoconductors devices exhibited visible wavelength responsivity up to 1.25×10^{3} $A \cdot W^{-1}$, specific detectivity up to 3.78×10^{12} $cm \cdot Hz^{1/2} \cdot W^{-1}$, and rise and fall times of 4.1 μs and 10.2 μs, respectively. Representative devices were also shown to maintain similar performance after 800 strain cycles. These results highlight the potential of strain tuneable InSe photoconductors for visible and NIR detection, paving the way for flexible and reconfigurable optoelectronic applications.

Supporting Information

DFT bulk-InSe bandgap simulations; InSe lifetime measurements; AFM thickness measurements; thickness dependent absorption simulations; profilometry measurement of strain to determine application method accuracy; Raman mapping of InSe under strain; detectivity calculations and noise current spectral density measurements; spectrally dependent responsivity, external quantum efficiency (EQE), absorption, and gain profiles; non-normalised strained responsivity spectra; InSe air exposure measurements.

Acknowledgements

L.P. acknowledges support from the Elizabeth and Vernon Puzey Scholarship. This project was supported by the Australian Research Council (ARC) under project DE210101129. J.B. acknowledges support from the Melbourne Centre for Nanofabrication through its Technology Fellow Program. This work was performed in part at the Melbourne Centre for Nanofabrication (MCN) in the Victorian Node of the Australian National Fabrication Facility (ANFF). J.A.H. acknowledges ARC programs CE170100026, LE210100151, and FT180100295.

Conflicts of interest

The authors declare no conflict of interest.

References

1. Huang, X., C. Liu, and P. Zhou, *2D semiconductors for specific electronic applications: from device to system.* npj 2D Materials and Applications, 2022. **6**(1).
2. Kang, S., D. Lee, J. Kim, A. Capasso, H.S. Kang, J.-W. Park, C.-H. Lee, and G.-H. Lee, *2D semiconducting materials for electronic and optoelectronic applications: potential and challenge.* 2D Materials, 2020. **7**(2): p. 022003.
3. Mak, K.F. and J. Shan, *Photonics and optoelectronics of 2D semiconductor transition metal dichalcogenides.* Nature Photonics, 2016. **10**(4): p. 216-226.
4. Bonaccorso, F., Z. Sun, T. Hasan, and A.C. Ferrari, *Graphene photonics and optoelectronics.* Nature Photonics, 2010. **4**(9): p. 611-622.
5. Chen, X., K. Shehzad, L. Gao, M. Long, H. Guo, S. Qin, X. Wang, F. Wang, Y. Shi, W. Hu, Y. Xu, and X. Wang, *Graphene Hybrid Structures for Integrated and Flexible Optoelectronics.* Advanced Materials, 2020. **32**(27): p. 1902039.
6. Jariwala, D., A.R. Davoyan, J. Wong, and H.A. Atwater, *Van der Waals Materials for Atomically-Thin Photovoltaics: Promise and Outlook.* ACS Photonics, 2017. **4**(12): p. 2962-2970.
7. Amani, M., D.-H. Lien, D. Kiriya, J. Xiao, A. Azcatl, J. Noh, S.R. Madhvapathy, R. Addou, S. Kc, M. Dubey, K. Cho, R.M. Wallace, S.-C. Lee, J.-H. He, J.W. Ager, X. Zhang, E. Yablonovitch, and A. Javey, *Near-unity photoluminescence quantum yield in MoS ₂.* Science, 2015. **350**(6264): p. 1065-1068.
8. Chaves, A., J.G. Azadani, H. Alsalman, D.R. Da Costa, R. Frisenda, A.J. Chaves, S.H. Song, Y.D. Kim, D. He, J. Zhou, A. Castellanos-Gomez, F.M. Peeters, Z. Liu, C.L. Hinkle, S.-H. Oh, P.D. Ye, S.J. Koester, Y.H. Lee, P. Avouris, X. Wang, and T. Low, *Bandgap engineering of two-dimensional semiconductor materials.* npj 2D Materials and Applications, 2020. **4**(1).
9. Chang, H.C., C.L. Tu, K.I. Lin, J. Pu, T. Takenobu, C.N. Hsiao, and C.H. Chen, *Synthesis of Large-Area InSe Monolayers by Chemical Vapor Deposition.* Small, 2018. **14**(39): p. 1802351.
10. Balakrishnan, N., E.D. Steer, E.F. Smith, Z.R. Kudrynskyi, Z.D. Kovalyuk, L. Eaves, A. Patanè, and P.H. Beton, *Epitaxial growth of γ -InSe and α , β , and γ -In.* 2D Materials, 2018. **5**(3): p. 035026.
11. Geng, J., D. Zhang, I. Kim, H.M. Kim, N. Higashitarumizu, I.K.M.R. Rahman, L. Lam, J.W. Ager Iii, A.V. Davydov, S. Krylyuk, and A. Javey, *Unusually Strong Near-Infrared Photoluminescence of Highly Transparent Bulk InSe Flakes.* Advanced Functional Materials, 2025. **35**(3): p. 2413672.
12. Jiang, J., L. Xu, C. Qiu, and L.-M. Peng, *Ballistic two-dimensional InSe transistors.* Nature, 2023. **616**(7957): p. 470-475.
13. Leisgang, N., J.G. Roch, G. Froehlicher, M. Hamer, D. Terry, R. Gorbachev, and R.J. Warburton, *Optical second harmonic generation in encapsulated single-layer InSe.* AIP Advances, 2018. **8**(10): p. 105120.
14. Sun, Y., S. Luo, X.-G. Zhao, K. Biswas, S.-L. Li, and L. Zhang, *InSe: a two-dimensional material with strong interlayer coupling.* Nanoscale, 2018. **10**(17): p. 7991-7998.
15. Mudd, G.W., M.R. Molas, X. Chen, V. Zólyomi, K. Nogajewski, Z.R. Kudrynskyi, Z.D. Kovalyuk, G. Yusa, O. Makarovsky, L. Eaves, M. Potemski, V.I. Fal'ko, and A. Patanè, *The direct-to-indirect band gap crossover in two-dimensional van der Waals Indium Selenide crystals.* Scientific Reports, 2016. **6**(1): p. 39619.
16. Zhao, Q., W. Jie, T. Wang, A. Castellanos-Gomez, and R. Frisenda, *InSe Schottky Diodes Based on Van Der Waals Contacts.* Advanced Functional Materials, 2020. **30**(24): p. 2001307.
17. Liang, G., Y. Wang, J. Zhang, Z.R. Kudrynskyi, Z. Kovalyuk, A. Patanè, Q. Xin, and A. Song, *High-Performance Phototransistors by Alumina Encapsulation of a 2D Semiconductor with Self-Aligned Contacts.* Advanced Electronic Materials, 2022. **8**(5): p. 2100954.

18. Yang, H.-W., H.-F. Hsieh, R.-S. Chen, C.-H. Ho, K.-Y. Lee, and L.-C. Chao, *Ultraefficient Ultraviolet and Visible Light Sensing and Ohmic Contacts in High-Mobility InSe Nanoflake Photodetectors Fabricated by the Focused Ion Beam Technique.* ACS Applied Materials & Interfaces, 2018. **10**(6): p. 5740-5749.
19. Huangfu, Z., J. Wang, X. Cheng, S. Feng, Y. Liang, C. Yuan, X. Zhu, Z. Wang, H. Zhang, and K. Yang, *The effect of different strain on the structural and optical properties of multilayer γ-InSe.* Journal of Alloys and Compounds, 2023. **961**: p. 170998.
20. Li, Y., T. Wang, M. Wu, T. Cao, Y. Chen, R. Sankar, R.K. Ulaganathan, F. Chou, C. Wetzel, C.-Y. Xu, S.G. Louie, and S.-F. Shi, *Ultrasensitive tunability of the direct bandgap of 2D InSe flakes via strain engineering.* 2D Materials, 2018. **5**(2): p. 021002.
21. Dai, M., H. Chen, F. Wang, Y. Hu, S. Wei, J. Zhang, Z. Wang, T. Zhai, and P. Hu, *Robust Piezo-Phototronic Effect in Multilayer γ-InSe for High-Performance Self-Powered Flexible Photodetectors.* ACS Nano, 2019. **13**(6): p. 7291-7299.
22. Gao, G.-L., D. Li, H.-L. Huang, and W. Xia, *Enhancement of electronic and optoelectronic performance of multilayer InSe via strain engineering.* Semiconductor Science and Technology, 2020. **35**(5): p. 055016.
23. Song, C., F. Fan, N. Xuan, S. Huang, G. Zhang, C. Wang, Z. Sun, H. Wu, and H. Yan, *Largely Tunable Band Structures of Few-Layer InSe by Uniaxial Strain.* ACS Applied Materials & Interfaces, 2018. **10**(4): p. 3994-4000.
24. Yang, S., Y. Chen, and C. Jiang, *Strain engineering of two-dimensional materials: Methods, properties, and applications.* InfoMat, 2021. **3**(4): p. 397-420.
25. Kim, H., S.Z. Uddin, D.-H. Lien, M. Yeh, N.S. Azar, S. Balendhran, T. Kim, N. Gupta, Y. Rho, C.P. Grigoropoulos, K.B. Crozier, and A. Javey, *Actively variable-spectrum optoelectronics with black phosphorus.* Nature, 2021. **596**(7871): p. 232-237.
26. Desai, S.B., G. Seol, J.S. Kang, H. Fang, C. Battaglia, R. Kapadia, J.W. Ager, J. Guo, and A. Javey, *Strain-Induced Indirect to Direct Bandgap Transition in Multilayer WSe₂.* Nano Letters, 2014. **14**(8): p. 4592-4597.
27. Matthewson, M.J., C.R. Kurkjian, and S.T. Gulati, *Strength Measurement of Optical Fibers by Bending.* Journal of the American Ceramic Society, 1986. **69**(11): p. 815-821.
28. Li, Z., Y. Lv, L. Ren, J. Li, L. Kong, Y. Zeng, Q. Tao, R. Wu, H. Ma, B. Zhao, D. Wang, W. Dang, K. Chen, L. Liao, X. Duan, X. Duan, and Y. Liu, *Efficient strain modulation of 2D materials via polymer encapsulation.* Nature Communications, 2020. **11**(1): p. 1151.
29. Lei, S., F. Wen, L. Ge, S. Najmaei, A. George, Y. Gong, W. Gao, Z. Jin, B. Li, J. Lou, J. Kono, R. Vajtai, P. Ajayan, and N.J. Halas, *An Atomically Layered InSe Avalanche Photodetector.* Nano Letters, 2015. **15**(5): p. 3048-3055.
30. Wang, S., A. Ashokan, S. Balendhran, W. Yan, B.C. Johnson, A. Peruzzo, K.B. Crozier, P. Mulvaney, and J. Bullock, *Room Temperature Bias-Selectable, Dual-Band Infrared Detectors Based on Lead Sulfide Colloidal Quantum Dots and Black Phosphorus.* ACS Nano, 2023. **17**(12): p. 11771-11782.
31. *Mackowiak, V., et al.NEP-Noise Equivalent Power, Vol. 56 (Thorlabs, Inc, 2015).*
32. Ghatak, S., A.N. Pal, and A. Ghosh, *Nature of Electronic States in Atomically Thin MoS2 Field-Effect Transistors.* ACS Nano, 2011. **5**(10): p. 7707-7712.
33. Lopez-Sanchez, O., D. Lembke, M. Kayci, A. Radenovic, and A. Kis, *Ultrasensitive photodetectors based on monolayer MoS2.* Nature Nanotechnology, 2013. **8**(7): p. 497-501.
34. Zhang, W., J.-K. Huang, C.-H. Chen, Y.-H. Chang, Y.-J. Cheng, and L.-J. Li, *High-Gain Phototransistors Based on a CVD MoS2 Monolayer.* Advanced Materials, 2013. **25**(25): p. 3456-3461.
35. Xu, H., J. Wu, Q. Feng, N. Mao, C. Wang, and J. Zhang, *High Responsivity and Gate Tunable Graphene-MoS2 Hybrid Phototransistor.* Small, 2014. **10**(11): p. 2300-2306.
36. Mudd, G.W., S.A. Svatek, L. Hague, O. Makarovsky, Z.R. Kudrynskyi, C.J. Mellor, P.H. Beton, L. Eaves, K.S. Novoselov, Z.D. Kovalyuk, E.E. Vdovin, A.J. Marsden, N.R. Wilson, and A. Patanè,

High Broad-Band Photoresponsivity of Mechanically Formed InSe–Graphene van der Waals Heterostructures. Advanced Materials, 2015. **27**(25): p. 3760-3766.
37. Luo, W., Y. Cao, P. Hu, K. Cai, Q. Feng, F. Yan, T. Yan, X. Zhang, and K. Wang, *Gate Tuning of High-Performance InSe-Based Photodetectors Using Graphene Electrodes.* Advanced Optical Materials, 2015. **3**(10): p. 1418-1423.
38. Yang, Z., W. Jie, C.-H. Mak, S. Lin, H. Lin, X. Yang, F. Yan, S.P. Lau, and J. Hao, *Wafer-Scale Synthesis of High-Quality Semiconducting Two-Dimensional Layered InSe with Broadband Photoresponse.* ACS Nano, 2017. **11**(4): p. 4225-4236.
39. Lien, D.-H., S.Z. Uddin, M. Yeh, M. Amani, H. Kim, J.W. Ager, E. Yablonovitch, and A. Javey, *Electrical suppression of all nonradiative recombination pathways in monolayer semiconductors.* Science, 2019. **364**(6439): p. 468-471.
40. Ghosh, S., A. Varghese, K. Thakar, S. Dhara, and S. Lodha, *Enhanced responsivity and detectivity of fast WSe2 phototransistor using electrostatically tunable in-plane lateral p-n homojunction.* Nature Communications, 2021. **12**(1): p. 3336.
41. Helmers, H., C. Karcher, and A.W. Bett, *Bandgap determination based on electrical quantum efficiency.* Applied Physics Letters, 2013. **103**(3): p. 032108.
42. Arora, H., Y. Jung, T. Venanzi, K. Watanabe, T. Taniguchi, R. Hübner, H. Schneider, M. Helm, J.C. Hone, and A. Erbe, *Effective Hexagonal Boron Nitride Passivation of Few-Layered InSe and GaSe to Enhance Their Electronic and Optical Properties.* ACS Applied Materials & Interfaces, 2019. **11**(46): p. 43480-43487.
43. Ho, P.-H., Y.-R. Chang, Y.-C. Chu, M.-K. Li, C.-A. Tsai, W.-H. Wang, C.-H. Ho, C.-W. Chen, and P.-W. Chiu, *High-Mobility InSe Transistors: The Role of Surface Oxides.* ACS Nano, 2017. **11**(7): p. 7362-7370.
44. Meng, J., J.J. Cadusch, and K.B. Crozier, *Detector-Only Spectrometer Based on Structurally Colored Silicon Nanowires and a Reconstruction Algorithm.* Nano Letters, 2020. **20**(1): p. 320-328.
45. Radatović, B., O. Çakıroğlu, V. Jadriško, R. Frisenda, A. Senkić, N. Vujičić, M. Kralj, M. Petrović, and A. Castellanos-Gomez, *Strain-Enhanced Large-Area Monolayer MoS2 Photodetectors.* ACS Applied Materials & Interfaces, 2024. **16**(12): p. 15596-15604.
46. Gant, P., P. Huang, D. Pérez de Lara, D. Guo, R. Frisenda, and A. Castellanos-Gomez, *A strain tunable single-layer MoS2 photodetector.* Materials Today, 2019. **27**: p. 8-13.
47. Pei, Y., Y. Kang, X. Zhou, M. Ma, M. Yang, D. He, W. Li, and X. Xiao, *Strain-Modulated Dominant Response Band of Self-Powered Photodetector Based on WSe2 Lateral PN Homojunction.* Small, 2024. **n/a**(n/a): p. 2410773.
48. Veeralingam, S., L. Durai, and S. Badhulika, *Facile Fabrication of P(Electrodeposition)/N(Solvothermal) 2D-WS2-Homojunction Based High Performance Photo Responsive, Strain Modulated Piezo-Phototronic Diode.* ChemNanoMat, 2019. **5**(12): p. 1521-1530.
49. Tai, X., Y. Chen, S. Wu, H. Jiao, Z. Cui, D. Zhao, X. Huang, Q. Zhao, X. Wang, T. Lin, H. Shen, X. Meng, J. Wang, and J. Chu, *High-performance ReS2 photodetectors enhanced by a ferroelectric field and strain field.* RSC Advances, 2022. **12**(8): p. 4939-4945.

Figures

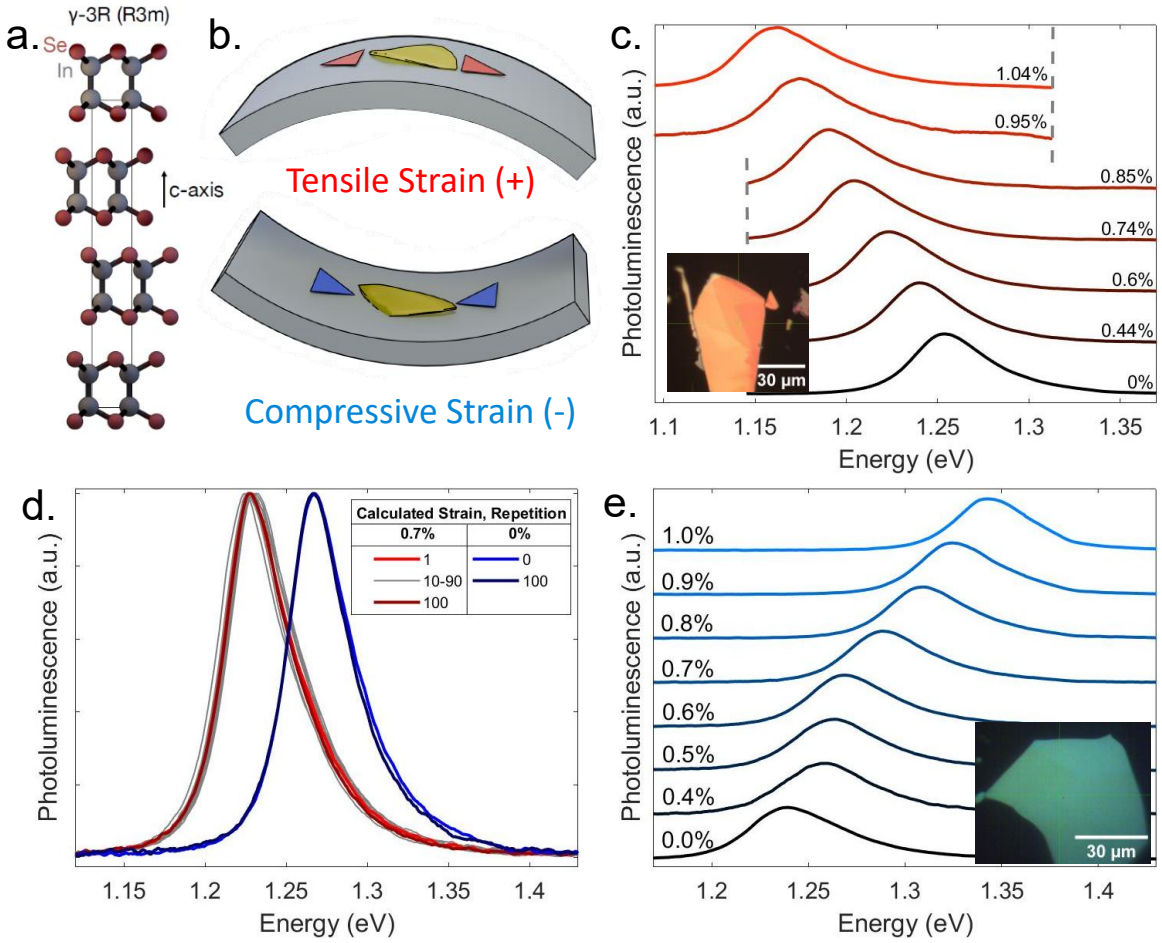

Figure 1: Strain application to bulk γ-InSe, (a) side-on view of γ-InSe crystal structure. (b) Schematic of how tensile and compressive strain are applied to the InSe flake (yellow). (c) Photoluminescence of bulk InSe under tensile strain from 0% to 1.04% calculated strain. The grey dashed lines in (c) mark the edge of the window for the PL measurement. (d) Photoluminescence at 0% and 0.7% tensile strain over 100 strain repetitions with blue curves at 0% strain and red curves at 0.7% tensile strain. (e) Photoluminescence of bulk InSe under compressive strain from 0% to 1% calculated strain. Inset in (c) and (e) are images of the InSe flakes measured, with a scale bar of 30 μm.

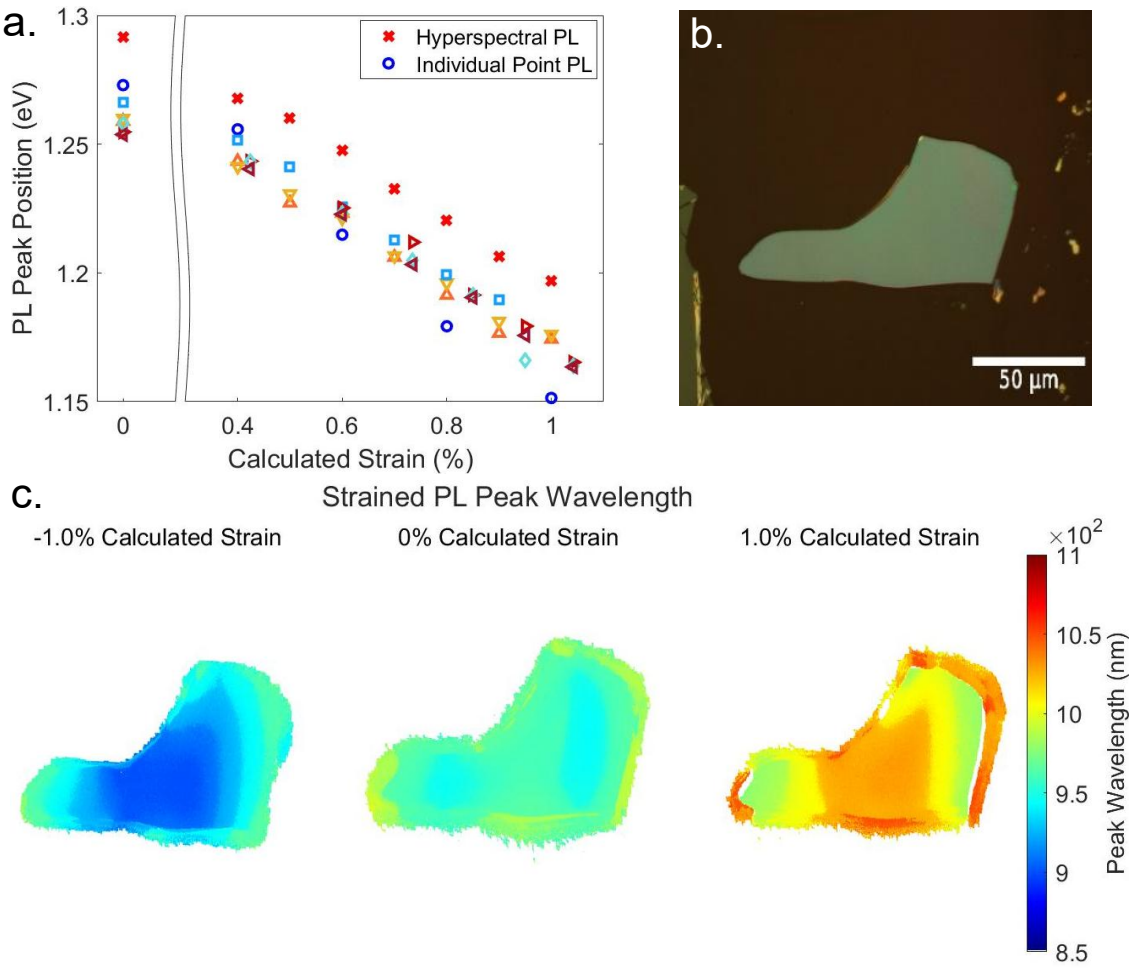

Figure 2: Additional photoluminescence characterisation under strain. (a) Collection of tensile strain PL peak position measurements from various bulk InSe samples along with the PL peak position from the hyperspectral measurement. Solid x-marker is for hyperspectral measurement and hollow markers are for all individual point measurements. (b) Optical microscope image of the InSe flake measured in (c). (c) Hyperspectral PL images of an InSe flake at -1%, 0%, and +1% strain. Colour represents PL peak emission wavelength.

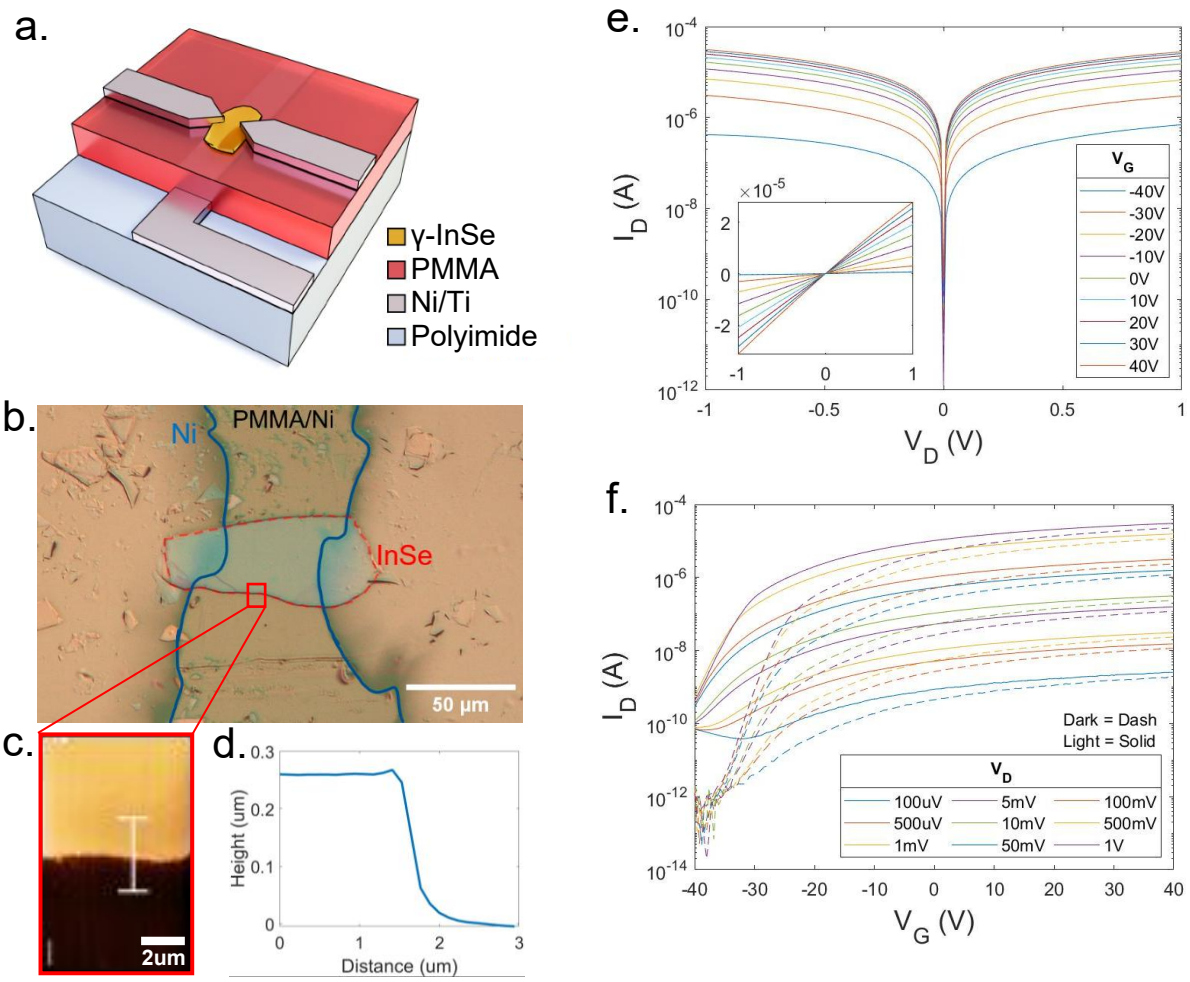

Figure 3: (a) Schematic of a gated InSe photoconductor device. (b) Optical microscope image of a representative InSe device, with a scale bar of 50 μm. (c) AFM topography of the highlighted area in (b), with a scale bar of 2 μm, and the height profile in (d) is extracted from white line in the image with the width of the line representing the area which the height profile is averaged across. (e) and (f) log scale plots of I_D vs. V_D and V_G respectively. Inset in (e) shows the same data on a linear scale showing linear behaviour. (f) also includes the I_D with no illumination and ~10 mW cm^{-2} white light illumination on the sample.

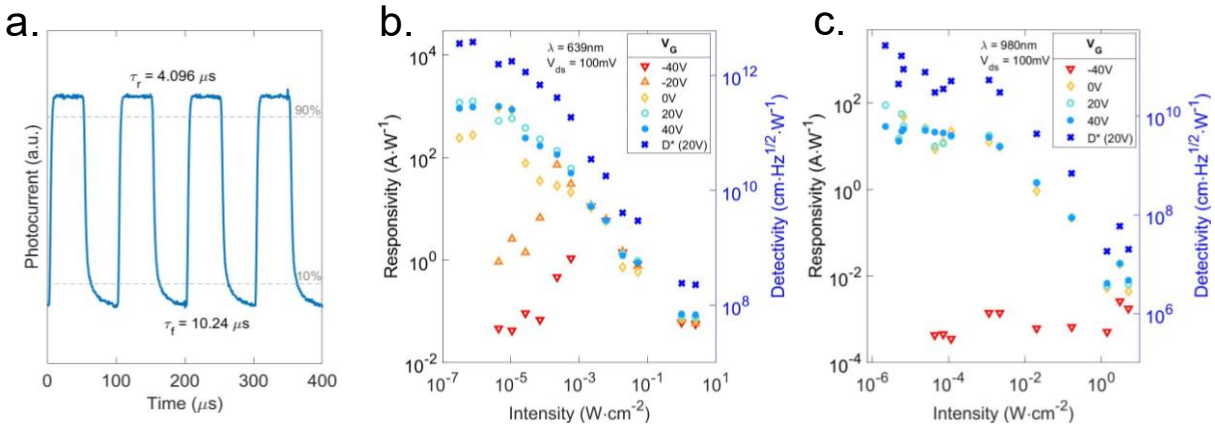

Figure 4: Photoconductor characterisation, (a) Measured unstrained photoresponse under λ = 639 nm illumination modulated at 10 kHz and the device biased with V_D = 100 mV and no V_G applied. Unstrained responsivity and detectivity measurement with an excitation source of λ = 639 nm (b) and λ = 980 nm (c) for varying illumination intensity. The gate bias was adjusted from -40 V to +40 V. The detectivity was only determined at V_G = +20 V (dark blue crosses). All measurements were taken at room temperature with V_D = 100 mV.

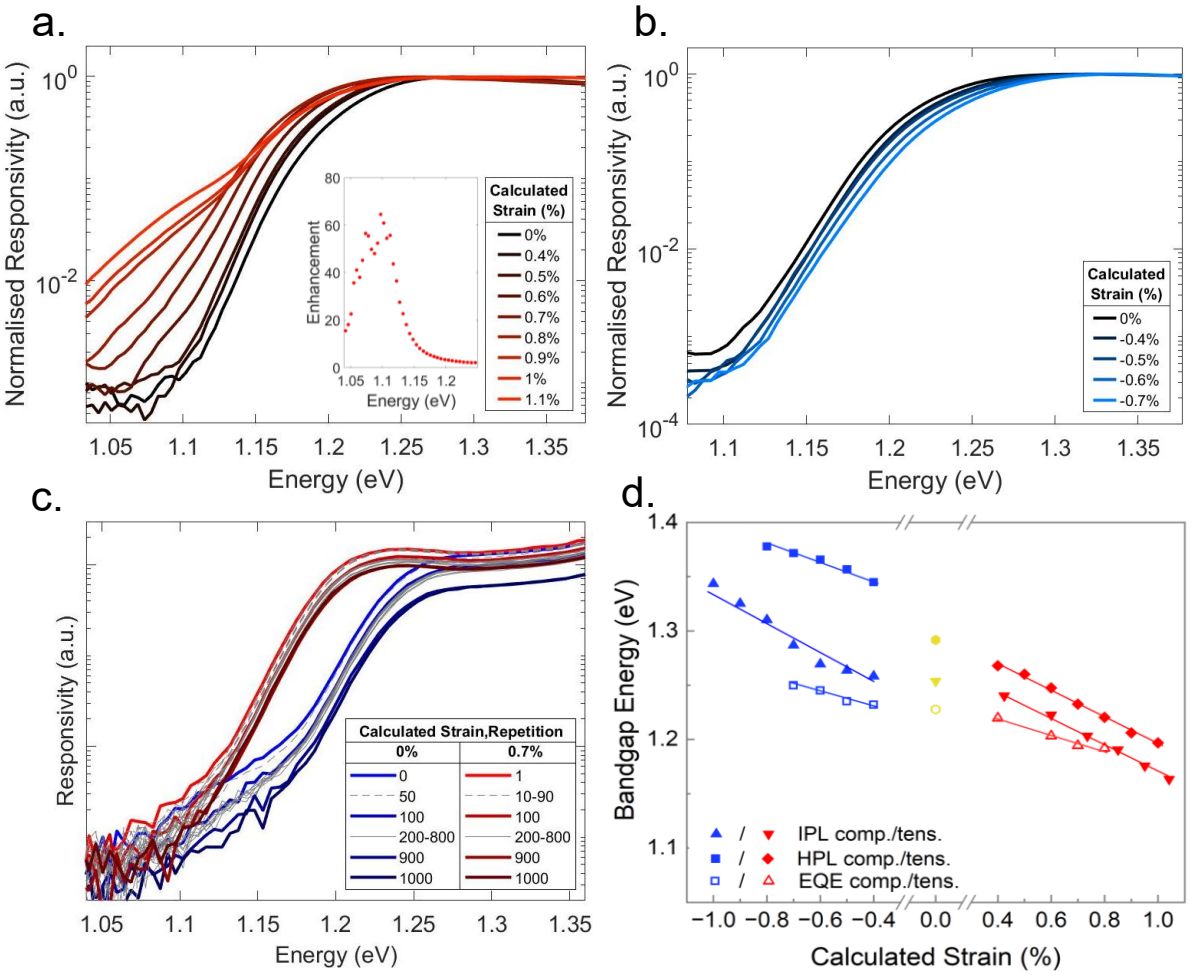

Figure 5: Spectral response measurements of representative strained InSe photoconductors. (a) and (b) show tensile and compressive strain from 0% to 1.1% and 0% to -0.7% respectively. Inset in (a) shows the enhancement in responsivity when switching from 0% to 1% tensile strain near the band edge. (c) Repeatability testing of tensile strain from 0% (blue lines) to 0.7% (red lines) over the course of 1000 strain repetitions (grey lines show all measured spectra at both strain values). (d) Collection of hyperspectral PL peak position (HPL, solid squares/diamonds), extracted bandgap from EQE measurements (PC, hollow shapes), and a representative tensile and compressive individual point PL (IPL, solid triangles). Compression = blue and tensile = red in PL and EQE measurements. Lines provide a guide to the eyes only.

Table 1: 2D material strain tunable photoconductors

*Substrate: PC (polycarbonate), PET (Polyethylene Terephthalate), PETG (Polyethylene Terephthalate Glycol), PI (Polyimide)
^Shift Rate: T (Tensile), C (Compression), PD (Photodetector), PL (Photoluminescence)

Material	**Substrate***	**Measurement Wavelengths (nm)**	**Bias (V)**	**Responsivity ($A \cdot W^{-1}$)**	**Detectivity ($cm \cdot Hz^{1/2} \cdot W^{-1}$)**	**Response Time (s)**	**Maximum Strain (%)**	**Shift Rate^ ($meV \cdot \%^{-1}$)**	**Ref.**
MoS_2	PC	400-700	1	5×10^{-3}	-	~4	0-1%	T: 51 (PD)	[45]
MoS_2	PC	450-800	10	200	-	80×10^{-3}	-1.44 - 0.48%	135 (PD)	[46]
WSe_2 Homojunction	PET	500-850	0	0.280	1.3×10^{12}	34×10^{-3}	0 - 1.04%	-	[47]
WS_2 Homojunction	PET	600	0.5	44.8	1.12×10^{13}	-	0 - 0.98%	-	[48]
ReS_2	PI	830	0.1	11.3	1.7×10^{10}	-	0 - 0.25%	-	[49]
bP	PETG	1300-5500	0.1	~2.8	8.45×10^{9}	18.7×10^{-6}	-0.66 – 1.21%	162 (PL) T: 157 (PD)	[25]
InSe	PET	400-800	0	0.825	1.7×10^{12}	20.3×10^{-6}	0 - 0.62%	-	[21]
InSe	PET	254-700	5	115.9	-	30×10^{-3}	0-1.06%	T: 58 (PL)	[22]
InSe	PET	840-1100	0.3	-	-	-	-0.62 - 1.06%	T: 154 (PL) T: 64 (PD) C: 140 (PL)	[20]
InSe	PI	639-1200	0.1	1.25×10^{3}	3.78×10^{12}	10.2×10^{-6}	-1 - 1.1%	T: 117.1 (PL) T: 44.5 (PD) C: 107.6 (PL) C: 35.1 (PD)	This Work

TOC Graphic

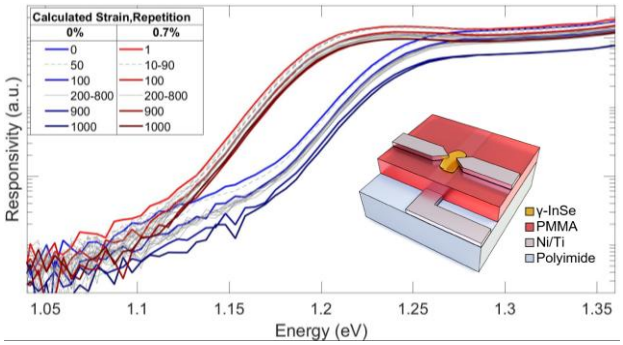
Calculated Strain,Repetition
0%
0.7%
0
50
100
200-800
900
1000
1
10-90
100
200-800
900
1000
Responsivity (a.u.)
1.05
1.1
1.15
1.2
1.25
1.3
1.35
Energy (eV)
γ-InSe
PMMA
Ni/Ti
Polyimide